



Numerical simulation of magnetic pulse radial compaction of W-Cu20 powder with a field shaper

Fenqiang Li¹ · Hui Li¹ · Xiaohong Ge¹ · Jun Zhao¹ · Huawei Wu¹ · Jia Lin¹ · Guimei Huang¹

Received: 21 October 2020 / Accepted: 1 March 2021 / Published online: 10 March 2021
© The Author(s), under exclusive licence to Springer-Verlag London Ltd., part of Springer Nature 2021

Abstract

The magnetic field in a magnetic pulse radial compaction process was analyzed in ANSYS/Multiphysical software to determine the electromagnetic force distribution on the driver tube. The node electromagnetic forces were then imported into the structure field as a boundary condition in ABAQUS/Explicit software. A modified Drucker-Prager Cap model was then established to reproduce the compaction behavior of W-Cu20 powder by writing a VUSDFLD subroutine. The Cowper-Symonds constitutive model was used to describe the deformation behavior of the driver tube, the pack tube, and the nylon terminal. Finally, the results predicted by numerical simulation were verified by experiment. The velocity, pressure variation, final distribution of relative density, and relative density uniformity during the magnetic pulse radial compaction process of W-Cu20 powder with a field shaper were predicted by the model, and the effect of field shaper on the relative density was analyzed. The results validate the numerical simulation model of magnetic pulse radial compaction. The magnetic pulse radial powder compaction with a field shaper can significantly increase the compacted compound density with the condition that the inner diameter height of the field shaper is greater than the powder filling height. Although the slit of the field shaper can cause an uneven density distribution after compaction, in the effective range of the field shaper, the density unevenness is minor under the described conditions, less than 4.1%.

Keywords Magnetic pulse radial compaction · W-Cu20 powder · Modified Drucker-Prager Cap · Density distribution

1 Introduction

The magnetic pulse radial compaction (MPRC) process is a dynamic compaction method in which the driver tube accelerates at a high speed and collides with the pack tube, compacting the powder in the pack tube. In this process, the spiral coil is directly discharged using a capacitor, then an eddy current is induced on the driver tube, creating a mutually repelling electromagnetic force between the coil and the driver tube. Unlike traditional compaction methods, electromagnetic pulse compaction is not limited by the strength of the pressing equipment. Electromagnetic pulse compaction can produce greater compacting pressures and increase the density of

compacted material [1]. The method is especially well-suited to compacting nanopowders that are difficult to form into wires, tubes, and other shaft parts.

Numerical simulation of electromagnetic pulse compaction has been the subject of a number of scholars, but that research has concentrated largely on electromagnetic axial pulse compaction. A simulation model of 2D current induced electromagnetic field was postulated by Li [2] using the ANSYS/Multiphysics module. Using results of the electromagnetic field simulation as the boundary conditions, the Ti-6Al-4V powder axial compaction model was formulated for the powder module of MSC.MARC, using Shima yield criterion. The effects of the discharge voltage, compaction temperature, and friction coefficient on the average relative density and uniformity of the compacted compound were analyzed. The deformation speed determined by analysis of the compaction model was designated as the boundary condition, then the microscopic deformation mechanism of the powder particles was analyzed using the Johnson-Cook constitutive model in MSC.MARC.

Cui et al. [3] used the Shima model in the MSC Marc software to model copper powder in 3D. They directly applied

✉ Fenqiang Li
lfq@xmut.edu.cn

¹ Fujian Provincial Key Laboratory of Functional Materials and Applications, School of Materials Science and Engineering, Xiamen University of Technology, Xiamen 361024, People's Republic of China

the displacement time measured by high-speed camera as the boundary conditions, and analyzed the axial electromagnetic pulse suppression in detail. This research resulted in determination of the rebound law after compaction.

Yan et al. [4] used the Johnson-Cook constitutive model in the LS-DYNA software to dynamically analyze Ag-Cu-Sn multi-component metal solder axial electromagnetic pulse compaction. The powder was modeled during the compaction using the discrete element method. The stress and strain distribution of the powder can be analyzed, but the density distribution cannot be obtained directly, and the initial distribution of the powder is difficult to model accurately.

Boltachev et al. [1, 5] utilized the granular dynamics method of electromagnetic radial pulse compression to establish a 3D numerical model of nanoceramic powder radial electromagnetic pulse compaction. They systematically analyzed the relationship between compaction pressure and densification rate and the effect of inertia on the compaction process.

In the numerical simulation of powder compaction, the Drucker-Prager Cap constitutive model is widely used to describe the compaction behavior of powder. Mamalis et al. [6, 7] was the earliest to experimentally use Drucker-Prager Cap in LS-DYNA3D to model Y-Ba-Cu-O superconducting powders. They simulated explosive compaction/cladding for fabricating superconducting Y-Ba-Cu-O ceramic/metal compositing grooved discs. The final dimensions of the compact, pressure, temperature, and density distributions during the entire cladding compaction process were predicted. The proposed model was validated by subsequent experimental results.

Han et al. [8] proposed a modified Drucker-Prager Cap constitutive model to quantitatively reproduce the compaction behavior of pharmaceutical powders. The model was implemented in ABAQUS by writing a user subroutine to determine the stress and density distribution during compression, decompression, and ejection.

Zhou et al. [9] used the modified Drucker-Prager Cap constitutive model in ABAQUS to analyze the residual stress distribution of Distaloy AE powder after compaction. Hu et al. [10] used the modified Drucker-Prager Cap constitutive model to analyze the rolling of W-Cu20 powder in ABAQUS. The density distribution obtained by numerical simulation was consistent with the experimental result. Zhou et al. [11, 12] defined the model parameters of the modified Drucker-Prager Cap constitutive model for the Ag57.6-Cu22.4-Sn10-In10 mixed metal powder, then simulated the mold compaction in ABAQUS. The pressure displacement curve is basically consistent with the experimental result. On this basis, a powder constitutive model considering friction factors was proposed and the influence of friction stress on compaction density distribution was analyzed.

W-Cu20 alloy has a number of excellent mechanical and electrical properties. These include high strength, high hardness, low thermal expansion, and good electrical conductivity.

The alloy is widely used in metallurgical machinery, electronic information, aerospace, and other fields [10]. In this paper, we describe a magnetic field model of the magnetic pulse radial compaction (MPRC) of W-Cu20 powder with a field shaper as established in ANSYS/Multiphysical software. The objective was initially to determine the magnetic field strength and distribution of the electromagnetic force. Then with the electromagnetic force as the boundary condition, a structure field model was created in ABAQUS/Explicit software to predict the velocity, pressure variation, final distribution of relative density, and relative density uniformity during the MPRC process. Then the effect of field shaper on the relative density was analyzed. In this structure field model, the modified Drucker-Prager Cap constitutive model was used to reproduce the behavior of W-Cu20 powder during the electromagnetic pulse compression forming process.

2 Methods

2.1 Finite element model of magnetic field

Using dimensions of the tool for MPRC shown in Fig. 1, a 3D geometric model of the electromagnetic field numerical simulation was entered into the 3D modeling software then imported into ANSYS/Multiphysics. The air model was written directly into ANSYS. The mold was meshed using the solid97 element as shown in Fig. 2.

Inasmuch as the pack tube is completely shielded by the driver tube and at a distance from the coil, it was ignored in the magnetic field simulation. Only the electromagnetic force on the driver tube is considered. In order to simulate an infinite space with a finite model, a boundary condition of parallel magnetic lines was applied to the outer boundary of the air mesh. The current-carrying conductor was used to model the coil, in which a voltage drop applied to one end of the coil is zero. The current degree of freedom at the other end of the coil is coupled, and the current load shown in Fig. 3 was applied. The materials used for the coil, field shaper, and driver tube are aviation aluminum alloy, chromium zirconium copper alloy, and A1050 aluminum alloy, respectively. The space-time distribution of the electromagnetic force on the driver tube is based on the electrical parameters of the materials, as shown in Table 1.

2.2 Finite element model of structure field

The geometric model of the structure field was established in the 3D modeling software using the dimensions shown in Fig. 1, then imported into the ABAQUS/Explicit software. The C3D8R element was used to mesh the driver tube, pack tube, powder, mandrel, and the fixed terminals, as shown in Fig. 4. The coefficient of friction between the driver tube, the pack tube,

Fig. 1 Dimensions of the magnetic pulse radial compaction tool

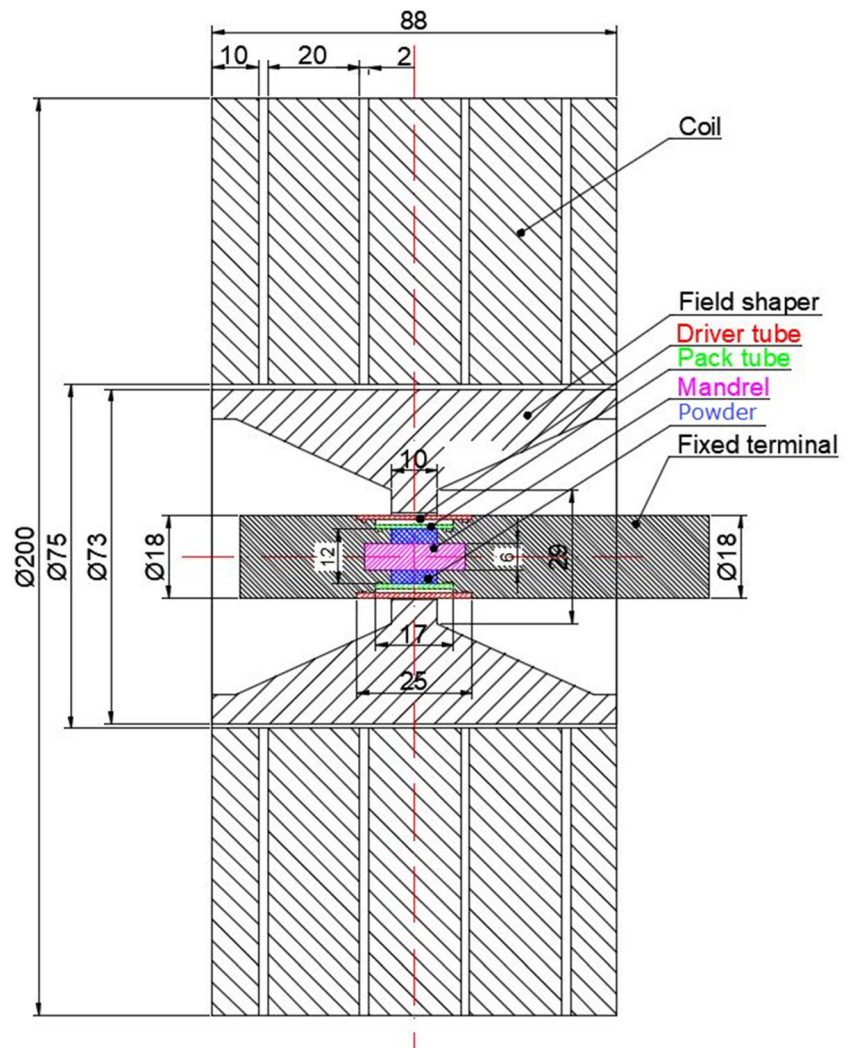
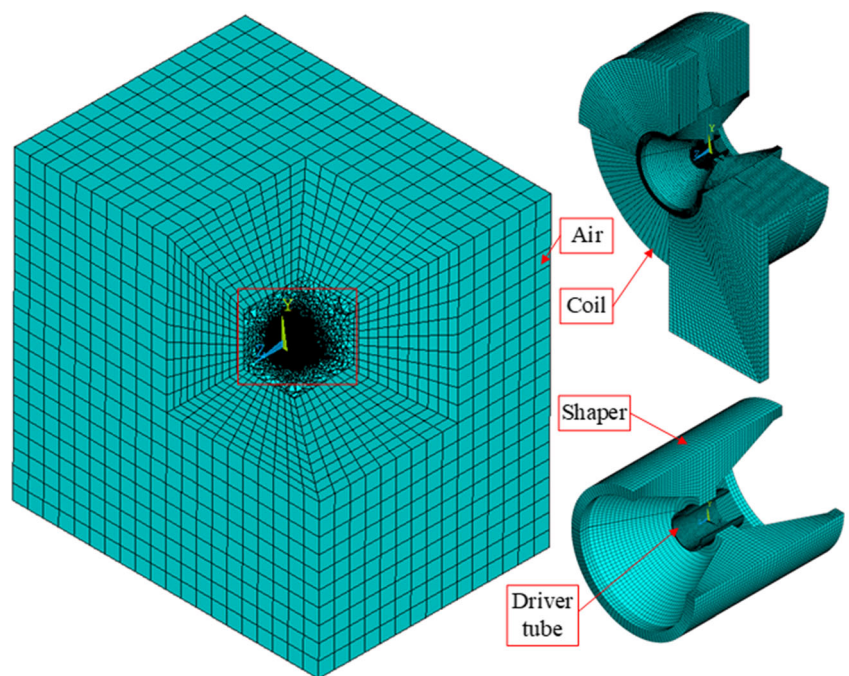


Fig. 2 Finite element model for electromagnetic field analysis



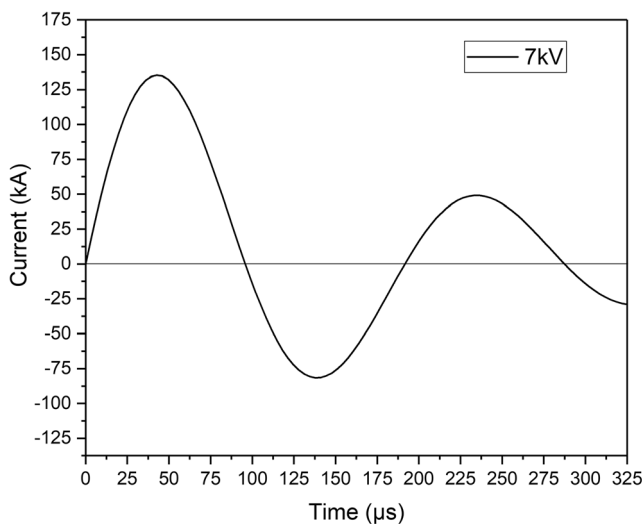


Fig. 3 The curve of current through the coil varying over time

the powder, and the mandrel was determined to be 0.12, and the coefficient of friction with the fixed terminals, 0.15. Fixed constraints were imposed on the outside end of the fixed terminals. The mesh of the driver tube is identical to the mesh of the driver tube in the magnetic field analysis. The nodal electromagnetic force determined by the magnetic field analysis can be directly applied to the structure field. The material compositions of the driver tube, pack tube, mandrel, and fixed terminal are aluminum alloy A1050, aluminum alloy A1050, stainless steel SUS304, and nylon PA6, respectively. MPRC is a high-speed forming process so the Cowper-Symonds constitutive model (Eq. 1) is used to assess the material strain rate effect. The mechanical properties of component materials are shown in Table 2. The true stress and true strain of the materials under quasi-static state are shown in Fig. 5.

$$\sigma = \left[1 + \left(\frac{\dot{\epsilon}}{C_m} \right)^{\frac{1}{p}} \right] \sigma_{Qs} \quad (1)$$

2.3 Modified Drucker-Prager Cap model

MPRC requires an accurate powder physical model and stipulated material parameters for structure field analysis. A modified Drucker-Prager Cap model (DPC) used in this paper as

Table 1 Electrical parameters of materials

Material	Relative permeability	Resistivity ($\times 10^{-8}$ ohm*m)
A7075	1.000022	5.22
CuCrZr	0.9999	2.17
A1050	1	2.78

shown in Fig. 6 consists of three parts: (1) Linear shear failure surface (also known as Drucker-Prager shear surface), to describe the stress limit of the material under shear. (2) Cap surface defines the relationship between yield stress and hydrostatic stress and inhibits the volume expansion caused by the material under shear. (3) The smooth transition surface, the main function of which is to connect shear destruction surface and Cap surface to facilitate convenient numerical calculation.

The main parameters of the modified DPC plastic model are β , d , R , α , pa , and pb . Except for α , the parameters are functions of relative density. In this paper, a DPC model based on relative density was established by writing the VUSDFLD subroutine in the ABAQUS/Explicit software to reproduce the W-Cu20 powder compaction behavior. Then the density and stress distribution in the powder compaction process were predicted. Among them, α is set to 0.2, and the relationship between the remaining material parameters and relative density is shown in Figs. 7, 8, 9, 10, and 11 [10].

The elastic modulus of the powder is calculated and determined according to formula (2) [10].

$$E = E_0 \rho^{0.5} \quad (2)$$

E_0 is the elastic modulus of compact body, and ρ is the relative density.

2.4 Experimental verification

The W-Cu20 powder used in the experiment was prepared by mixing ultra-fine high-purity tungsten powder with copper powder in a mass ratio of 4:1. Both materials were produced by China Metallurgical Research Institute. The experimental device is shown in Fig. 12, including an energy storage cabinet (including four sets of capacitors, $C = 740 \mu\text{f}$), a control cabinet, and a workbench. The workbench is equipped with radial compression coils and a field shaper. Established and accepted research determined that low-frequency long pulses are beneficial to powder compaction so multi-turn coils were used in this experiment, as shown in Fig. 1. The nylon fixed terminal, stainless steel mandrel, aluminum alloy pack tube, and aluminum alloy driver tube were fabricated to the dimension requirements shown in Fig. 1. Before MPRC, the stainless steel mandrel and aluminum alloy pack tube were installed on the nylon fixed terminal. The W-Cu20 powder was loaded between the pack tube and the mandrel and vibration were employed to increase the initial packing density. The driver tube and another fixed terminal were sealed off tightly, then the weight was measured to calculate the initial packing density. The assembled tool was installed in the field shaper and the position adjusted to ensure that the powder was contained within the full height of the inner diameter of the field shaper. A 7 kV discharge voltage was used for compaction. A Rogowski

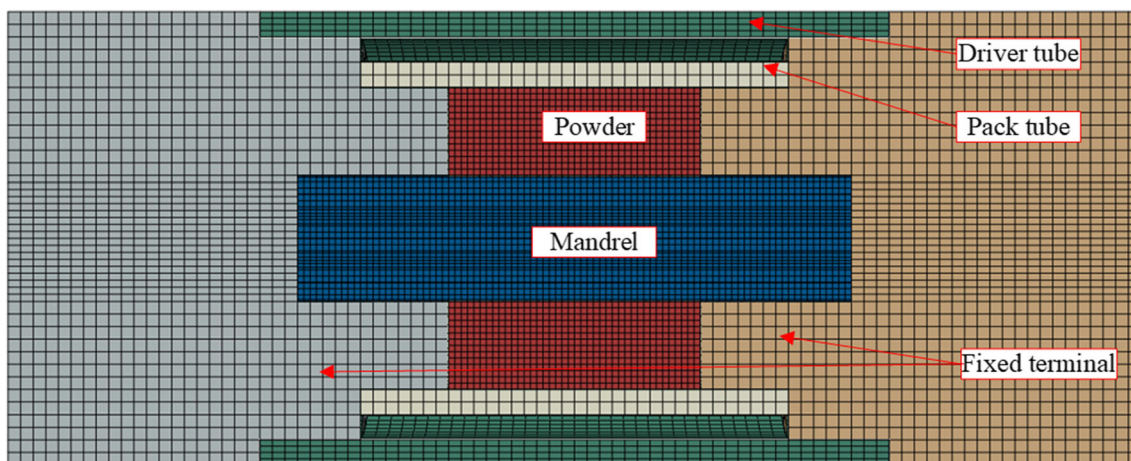


Fig. 4 Finite element model for structural field analysis

coil measured the current flowing through the coil. After compaction, ImageJ software was used to measure the diameter of the driver tube at several different points to calculate the deformation displacement of the driver tube and the density distribution of the W-Cu20 powder.

The appropriate calculation method [16] was used to determine compression density, assuming that the quality before and after compression is unchanged,

$$\begin{aligned}
 \text{then, } m &= V_0\rho_0 = \rho_0h\pi(r_{p0}^2-r_{m0}^2) = V\rho \\
 &= \rho h\pi[(r_d-t_d)^2-r_{m0}^2] \tag{3}
 \end{aligned}$$

- where r_{p0} —The initial outer diameter of the pack tube;
 - r_{m0} —the initial outer diameter of the mandrel;
 - r_d —the outer diameter of the driver tube after deformation;
 - t_d —the thickness of driver tube;
 - ρ_0 —initial relative density;
 - h —powder height;
 - ρ —the relative density after compaction.
- From Eq. (3),

$$\rho = \rho_0 \frac{r_{p0}^2-r_{m0}^2}{(r_d-t_d)^2-r_{m0}^2} \text{ can be obtained.} \tag{4}$$

Figure 13 is a comparison of the relative density distribution of the outer powder layer based on numerical simulation and that calculated by Eq. (4) using the outer diameter of the driver tube after experimental compaction.

As shown in Fig. 13, the numerical simulation and the calculated value of the experimental measurement are comparable. The maximum displacement of the driver tube predicted by the numerical simulation is slightly larger than the one measured experimentally, ignoring the effect of deformation on the magnetic field. Thus, the density predicted by the numerical simulation is slightly greater than the actual density determined by the experiment.

The relative density calculated by measuring the outer diameter of the driver tube according to Eq. (4) in the experiment is slightly greater than the actual relative density of the powder surface layer. The reason for this difference is that Eq. (4) ignores the mandrel deformation and the compression plastic deformation caused when the driver tube collides with the pack tube. Thus, the relative density predicted by numerical simulation is actually closer to the relative density calculated by using measurements in the experiment. It therefore can be argued that the multiphysics coupling model for MPRC established in this paper is reliable and can accurately predict the relative density distribution of powder after compaction.

3 Results and discussion

3.1 Magnetic field analysis

After the coil discharged for 38.32 μs , the electromagnetic force on the driver tube approached the maximum value.

Table 2 Material mechanical performance parameters

Material	Elastic modulus (GPa)	Poisson's ratio	Density (kg/m ³)	Yield strength (MPa)	C_m	p
A1050[13]	69	0.32	2700	247	6500	4
PA6[14]	8.3	0.28	1145	96	3190	2.59
SUS304[15]	195	0.247	7800	205	600	4.4

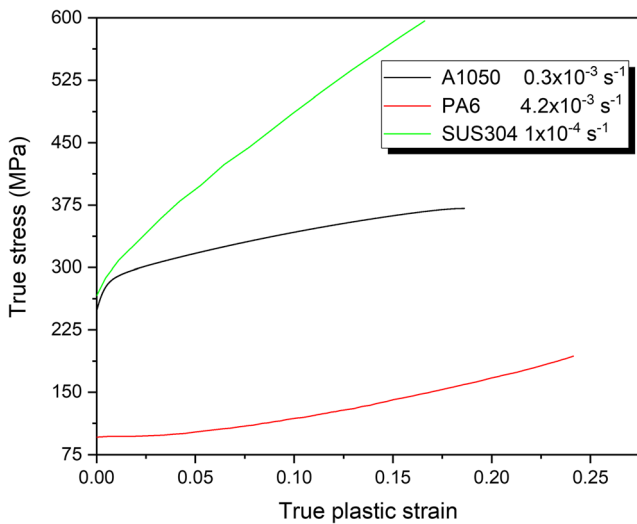


Fig. 5 True plastic stress-strain curves of specific materials under quasi-static conditions

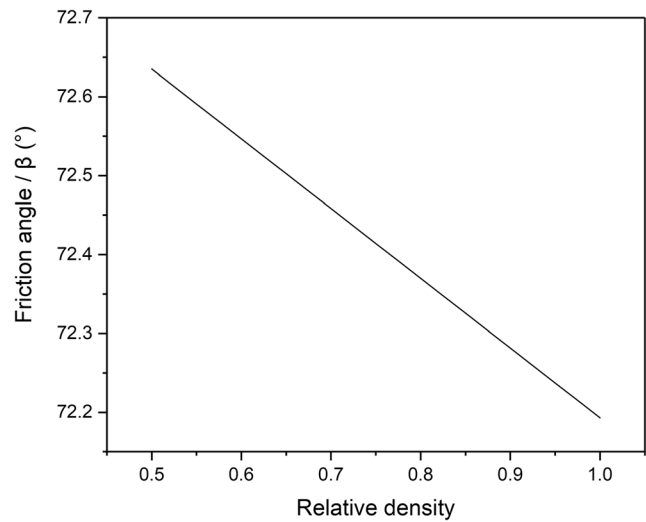


Fig. 7 The relationship between friction angle β and relative density

Figure 14 indicates the electromagnetic force imposed at different radial thicknesses of the driver tube, changing with the location in the z-axis direction at that instant.

The electromagnetic force reached its maximum on the side nearest the field shaper (outside), and minimum on the side most distant from the field shaper (inside). The inner diameter height of the field shaper used is 10 mm. The electromagnetic force on the outside of the driver tube within the working range of the field shaper (between the two red lines) is clearly greater than at other positions. The magnetic collecting effect is therefore obvious. The electromagnetic force on the driver tube gradually decreased at the two ends of the inner diameter of the field shaper due to the end effect.

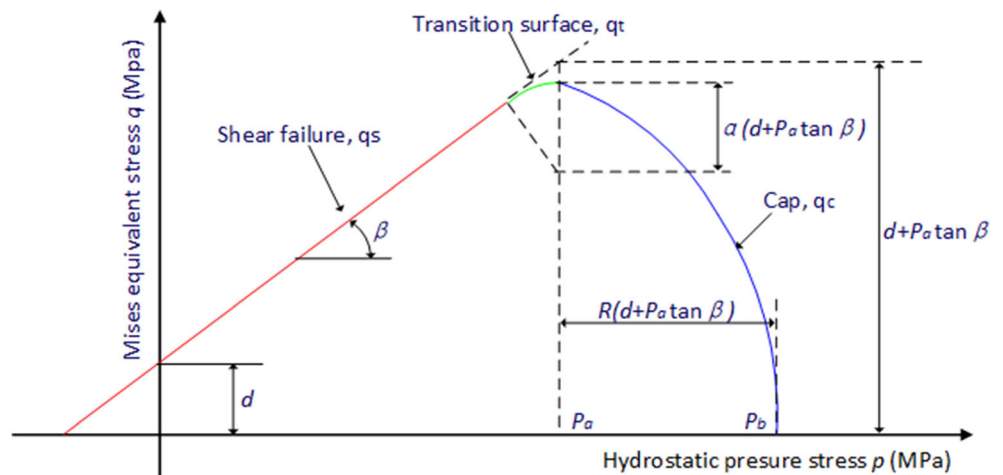
Figure 15 diagrams the electromagnetic force distribution at different circumferential points on the driver tube when subjected to a discharge for 38.32 μ s. The graphic shows that the electromagnetic force on the driver tube near the slit is

approximately 68 N, while the electromagnetic force at the location perpendicular to the slit is roughly 83 N. This is explained by the existence of small gaps in the junction of the two field shaper segments, so the electromagnetic force is slightly uneven in the circumferential distribution. This example further illustrates the importance of using a 3D model for analysis.

Figure 16 illustrates change of magnetic flux density over time at different radii and center of the axis of the tool. At the corresponding location of the inner diameter of the coil, the large and small diameters of the field shaper, the magnetic flux density changes over time and is basically synchronous with the discharge current, which first increases then decreases in the half cycle.

The frequency of the increase and attenuation of the magnetic flux density at the outer diameter of the driver tube is greater than that at other positions. Note that the field shaper increased the magnetic flux density by approximately 1.5.

Fig. 6 Schematic diagram of Drucker-Prager Cap model [8]. p , hydrostatic stress; q , equivalent stress; β , friction angle; d , cohesion; R , eccentricity; α , shape parameters, which determine the shape of the transition zone; pa , evolution parameter, the value of the intersection of the cap surface and the transition surface; pb , compression yield average stress, control the size of the cap surface



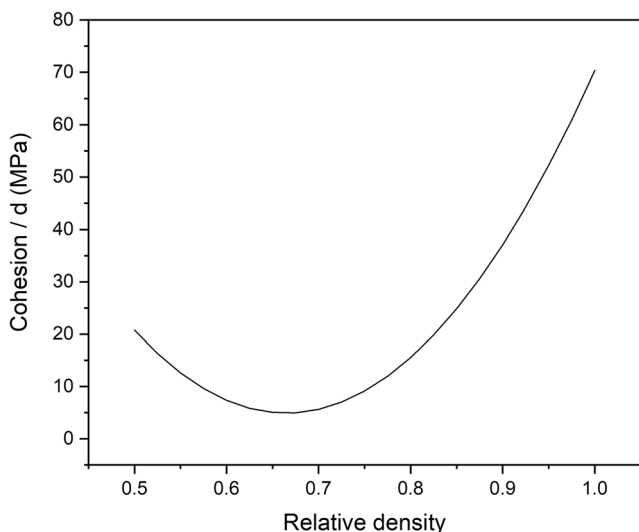


Fig. 8 Relationship curve between cohesion d and relative density

Distribution of the magnetic flux density in the center plane prior to reaching $69.4 \mu\text{s}$ gradually increased, rising from the location of the inner diameter of the coil to the outer diameter of the field shaper to the inner diameter of the field shaper and then to the outer diameter of the driver tube. The flux density increase at the outer diameter of the driver tube was significantly greater than that effecting the other positions.

It should be noted that the magnetic flux density at the outer diameter of the driver tube decays more rapidly than at other positions. Each measurement at points along the outer diameter of the driver tube is less than its corresponding location at other positions.

Figure 17 shows that magnetic flux density on different radial thicknesses and center of the axis of the driver tube varies over time. The magnetic flux density of the driver tube

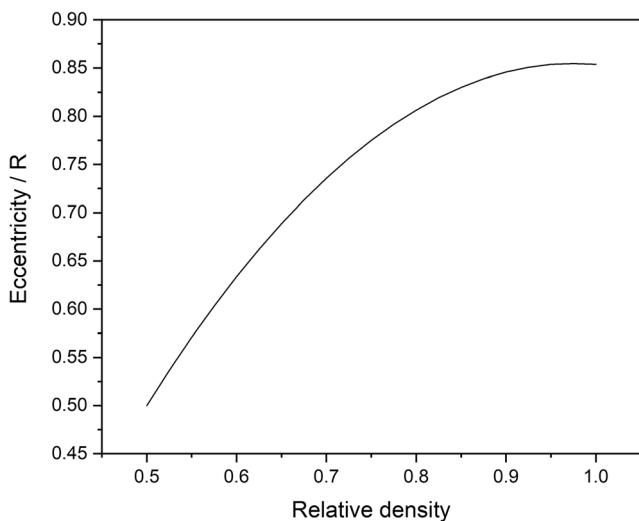


Fig. 9 The relationship between eccentricity R and relative density

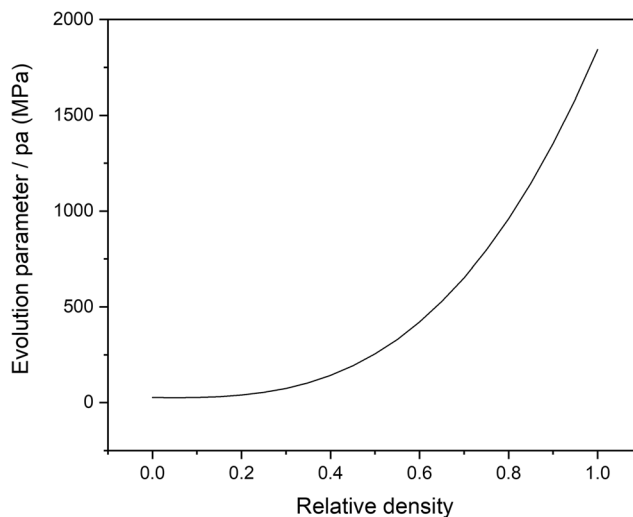


Fig. 10 The relationship between evolution parameter Pa and relative density

gradually decreased from outside to inside within the wall thickness range. Due to inconsistent frequency, after the elapsed discharge time reached $75 \mu\text{s}$, flux density gradually increased from the outside to the inside.

3.2 Structural field analysis

(1) Density distribution

Figure 18 graphically illustrates the relative density distribution of the tubular compound at different times. The relative density of the compound during the MPRC process was gradually compacted from outside to inside, with the result that maximum density occurred at the outer layer. Due to the end effect of the field shaper and the friction effect at the fixed end,

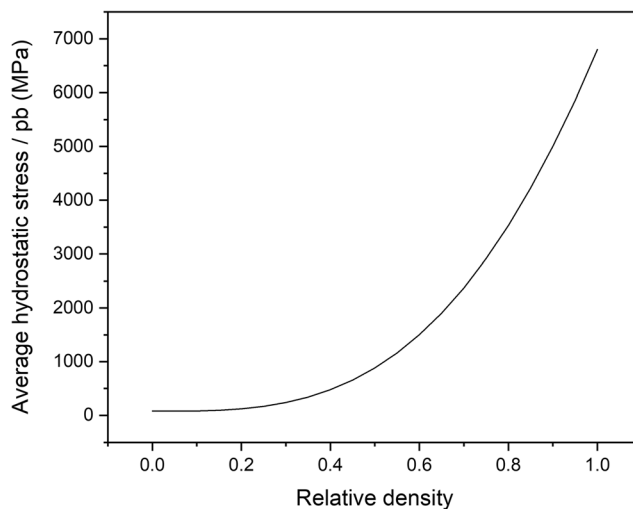


Fig. 11 The relationship between average hydrostatic stress Pb and relative density



Fig. 12 Experimental equipment

powder in the axial direction was gradually compacted from the center to the two ends, with the greater density concentrated in the middle section. Figure 19 records the final density distribution of the tubular compound in Fig. 18, with three paths subjected to detailed analysis. The red solid line

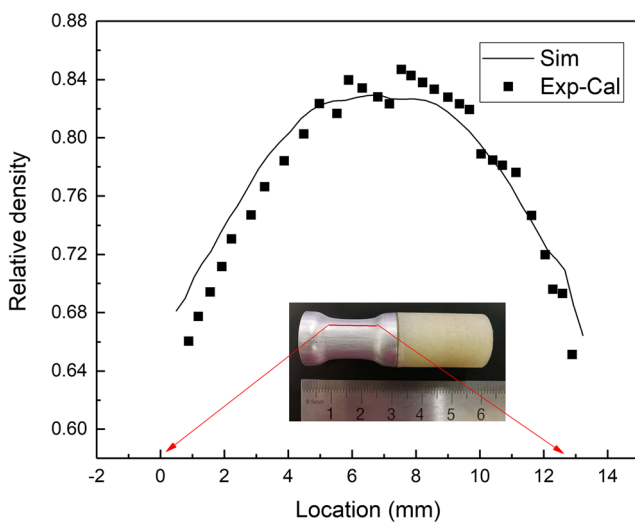


Fig. 13 Comparison of the relative density calculated from the outer diameter of the experiment driver tube and that obtained from the simulation

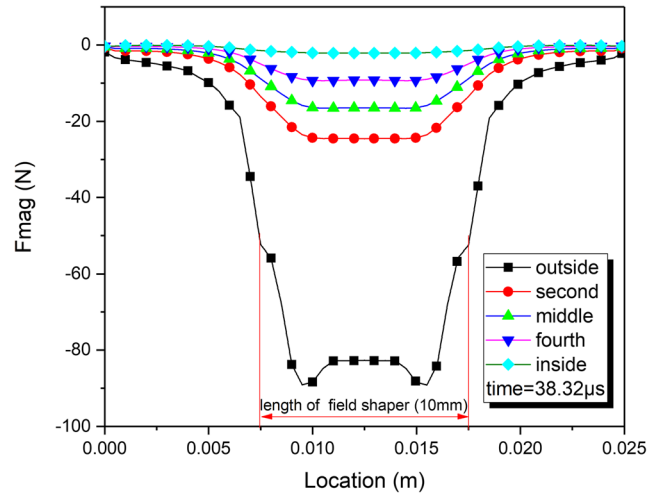


Fig. 14 Electromagnetic force distribution at different z-axis positions on the driving tube after discharge for 38.32 µs (negative value indicates radial compression)

represents the relative density distribution after compaction at different points in the axial direction. The blue dash line represents the relative density distribution in different thicknesses of the end. The green dotted line indicates the relative density distribution of different thicknesses in the center. The final density distribution is arc shaped and the density of the tubular compound is increasingly dense and uniform in the range of about 5 mm to the left and right of the midplane. It is submitted that the height of the inner diameter of the field shaper should be greater than the powder filling height or, alternatively, a progressive compaction process should be adopted in order to obtain a uniform, high-density tubular compound. The density distribution in thickness after

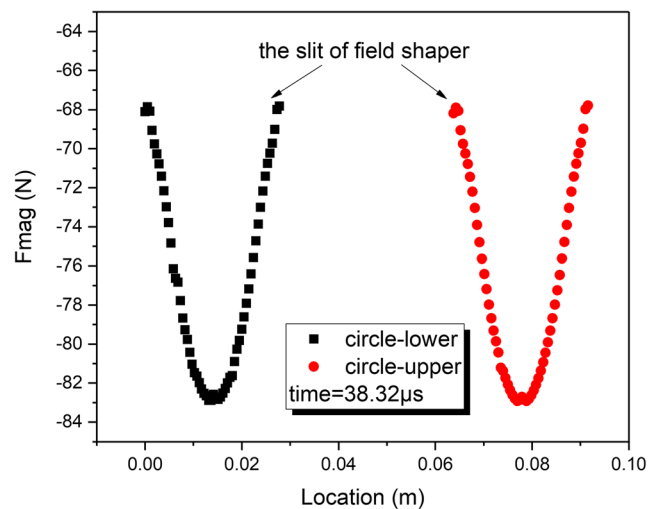


Fig. 15 Electromagnetic force distribution at different circumferential positions on the driver tube when subjected to a discharge of 38.32 µs (negative value indicates radial compression)

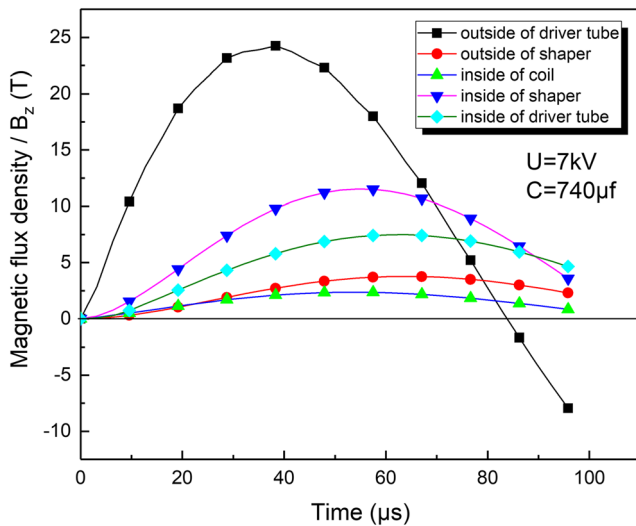


Fig. 16 Magnetic flux density variance at different radial positions (center in the axis) as a function of time

compaction is greatest nearest the mandrel. Clearly, the mandrel has the effect of improving the density of the powder.

Figure 20 graphs the distribution of relative density along the circumference of the center section of the blank after compaction. The red dotted line represents the relative density distribution of the inner diameter of the tubular compound. The relative density along the inner diameter is evenly distributed. The average relative density is 83.2% with a standard deviation of 0.37%. The black solid line charts the relative density distribution of the outer diameter of the tubular compound, characterized by substantial fluctuation in the relative density distribution. The average relative density is 81.7% and the standard deviation is 1.26%. These results are explained by the use of the field shaper for radial compression forming. Two small gaps in the junction of the two field shaper

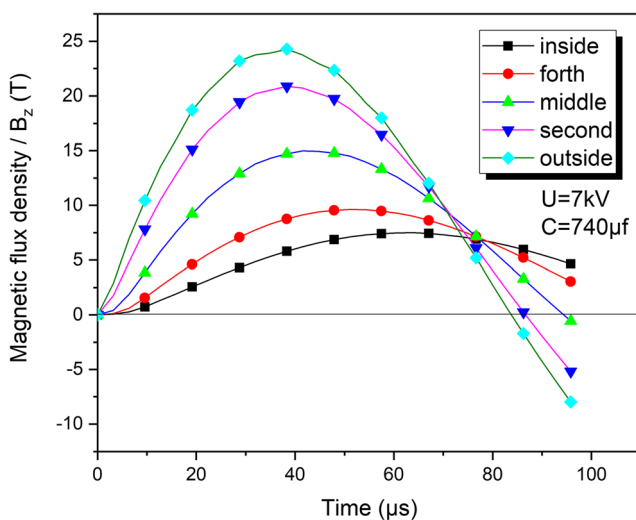


Fig. 17 Magnetic flux density at different driver tube thickness points varying over time

segments caused magnetic flux leakage and a reduction in the electromagnetic force during the forming process. As a result, relative density after compaction was less (corresponding to 0.5π and 1.5π location in the figure) and fluctuation in the relative density distribution occurred at the outer diameter, but less than 4.1%. It can be obtained that the relative density difference between the inner and outer diameters is greatest at the two gaps (corresponding to 0.5π and 1.5π location in the figure). It can be concluded that the center section of the tubular compound is basically uniform viewed from either the circumferential or the radial direction.

(2) Impact velocity

Figure 21 graphically displays the deformation speed of the driver tube, the pack tube, and the outer and inner surfaces of the tubular compound over time during the compaction process. The black solid line represents the deformation speed of the driver tube. The plot shows that after discharge, the driver tube accelerated for 13 μs , at which point the speed reached 219.81 m/s, where it collided with the pack tube (red dash) and began to decelerate. The tube then began to accelerate, reaching a speed of 113.92 m/s. The outer diameter of the powder then contacted the pack tube and accelerated to 185.96 m/s. The driver tube and pack tube were driven together to compact the powder by inertia. From prior analysis (Fig. 17), it could be obtained that the electromagnetic force on the driver tube at 75 μs gradually decreased from outside to inside, then gradually increased. At that point, the deformation speed of the driver tube began to oscillate, but the oscillation had no effect on the deformation speed of the tubular compound.

(3) Shock pressure

Figure 22 graphs impact pressure varying over time when the center position in the z-axis of the driver tube collided with the pack tube.

Peak pressure, as shown, is close to 3 GPa at impact. In combination with the data in Fig. 18, it can be determined that the preponderance of the compaction result was achieved at 1.5 GPa. The data argue persuasively that electromagnetic radial pulse compaction using a coil with a field shaper increases the magnetic flux density substantially, generating a greater compaction pressure and density of the tubular compound without damage to the equipment.

4 Conclusions

A modified Drucker-Prager Cap model was developed to describe the powder compaction process by writing a VUSDFLD subroutine in the ABAQUS software. The

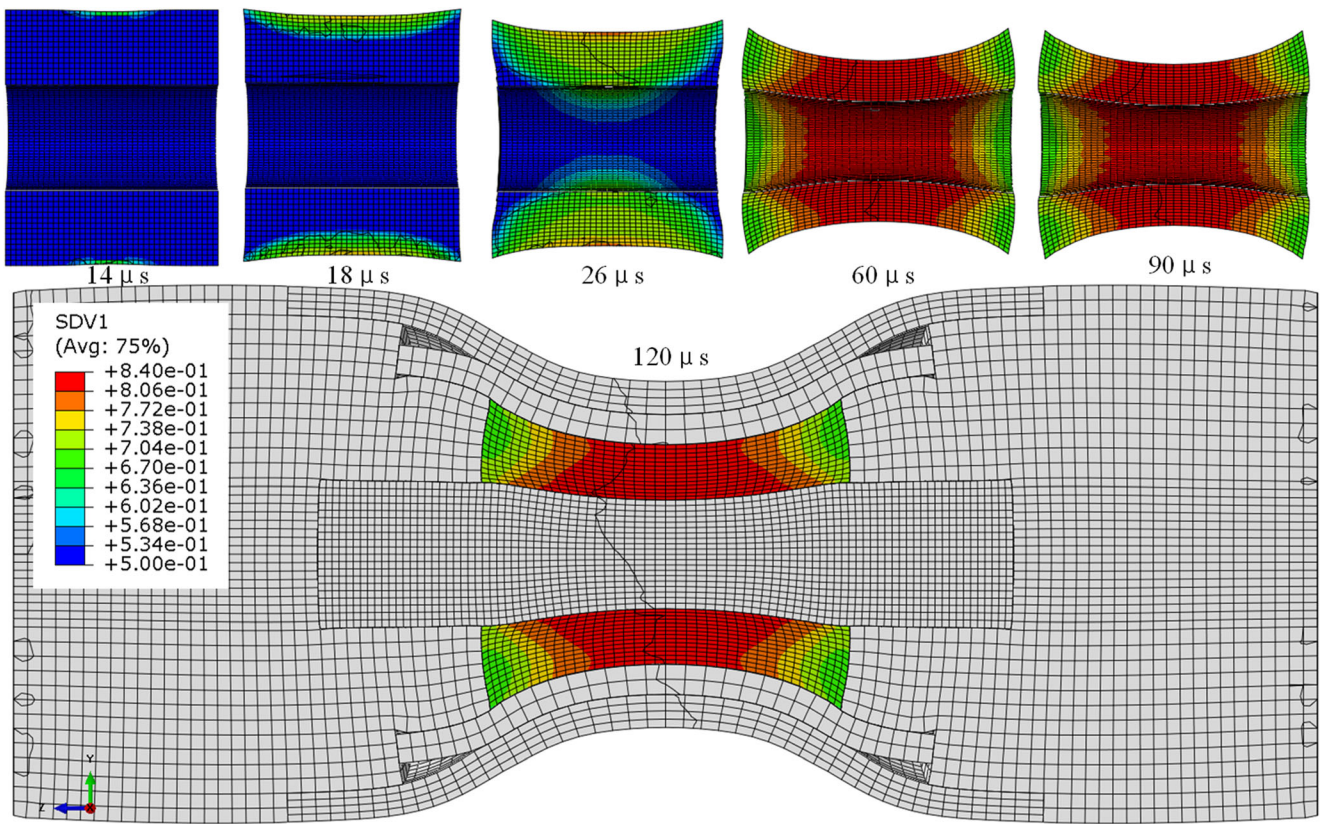


Fig. 18 Relative density distribution in tubular compound over time

electromagnetic force was calculated in ANSYS/Multiphysical, and applied as the boundary condition of the structure field to simulate in ABAQUS/Explicit. A 3D multiphysics numerical simulation model of MPRC of W-Cu20 powder was accomplished. Then the velocity, pressure

variation, final distribution of relative density, and relative density uniformity during MPRC of W-Cu20 powder with a field shaper were predicted by the model and the effect of field shaper on the relative density was analyzed. The conclusions are as follows:

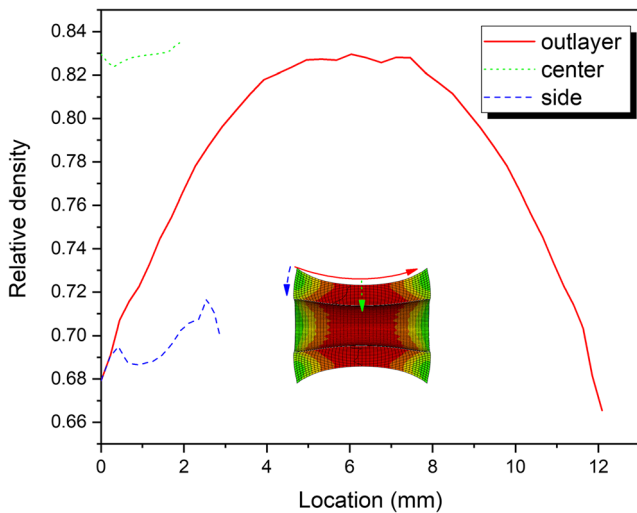


Fig. 19 Relative density distribution along three different paths

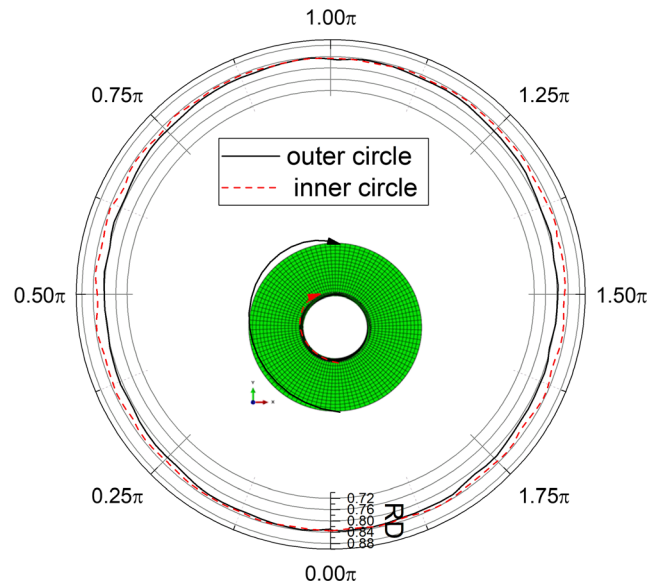


Fig. 20 Distribution of the relative density of the tubular compound in the circumferential direction

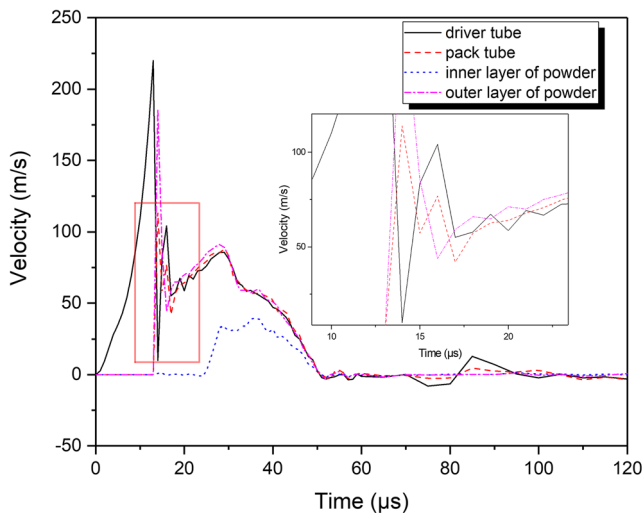


Fig. 21 Deformation speed of the driver tube, pack tube, outer surface, and inner surface of powder during compaction process over time

- (1) When compared with the experimental data, the 3D multiphysics numerical simulation model of MPRC in this paper is proven to be valid and can be used to reliably predict the stress and density distribution after MPRC.
- (2) Using a field shaper in electromagnetic pulse radial powder compaction results in concentration of the magnetic effect, significantly increasing the compact force while increasing the density. The height of the inner diameter of the field shaper should be greater than the powder filling height.
- (3) When the field shaper was used to enhance electromagnetic pulse radial powder compaction, slits on the field shaper caused uneven distribution of the electromagnetic force on the circumference of the driver tube, resulting in

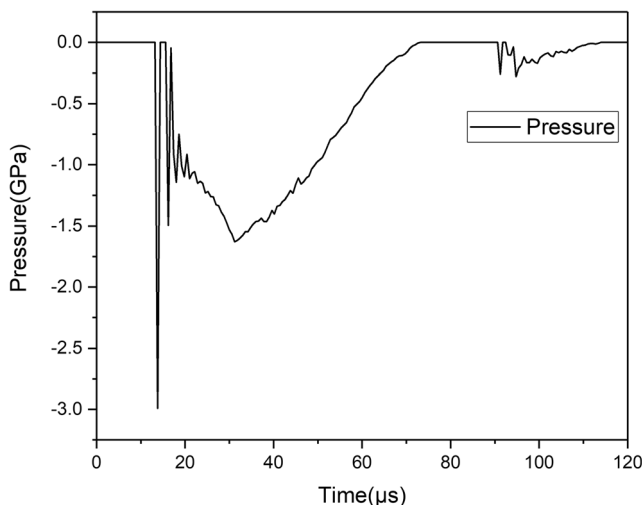


Fig. 22 Impact pressure over time when the center position in z-axis of the driver tube impacts the pack tube

uneven density distribution of the compacted body. Unevenness within the effective range of the field shaper is small, however, not exceeding 4.1%.

- (4) Electromagnetic pulse radial powder compacting process used to compact W-Cu20 tubular compound, with discharge voltage 7 kV, maximum compaction pressure reached 3 GPa with a maximum compaction speed of approximately 114 m/s. Relative density after compaction was 83.2%.

Author contribution Fenqiang Li: Writing, methodology, and investigation. Hui Li: Investigation. Xiaohong Ge: Funding acquisition. Jun Zhao: Formal analysis and investigation. Huawei Wu: Investigation. Jia Lin: Investigation. Guimei Huang: Investigation.

Funding This work was supported by the “Scientific Research Climbing Plan” (Grant No. XPDKQ18008) and Innovation Development Fund Project (Grant No. 49919014) of Xiamen University of Technology.

Data availability The data that support the findings of this study are openly available in [cnki.net] at <http://10.19591/j.cnki.cn11-1974/tf.2017.04.002>, reference number [10].

Code availability Thanks to ANSYS and Dassault Companies for providing software support.

Declarations

Ethics approval and consent to participate The manuscript has not been submitted to any other journal for simultaneous consideration. The submitted work is original and has not been published elsewhere in any form or language. All authors voluntarily agree to participate in this research study.

Consent for publication All authors voluntarily agree to the publication of the paper.

Conflict of interest The authors declare no conflict of interest.

References

1. Boltachev GS, Chingina EA, Spirin AV, Volkov NB (2019) Densification rate influence on nanopowder compactibility. *Mater Phys Mech* 42(2):165–177. https://doi.org/10.18720/MPM.4222019_2
2. Li M (2011) Microstructure and properties of Ti6Al4V alloy prepared by magnetic pulse compression and sintering of hydrogenation powder. Harbin Institute of Technology, Harbin
3. Cui J, Huang X, Dong D, Li G (2020) Effect of discharge energy of magnetic pulse compaction on the powder compaction characteristics and spring back behavior of copper compacts. *Met Mater Int*. <https://doi.org/10.1007/s12540-020-00698-6>
4. Yan S, Lei Y, Huang S, Wang Q, Zhou M, Hu J, Zou F (2019) Dynamic analysis of electromagnetic compaction of Ag-Cu-Sn multivariate mixed metal powders for brazing. *Int J Appl Electromagn Mech* 60:457–476. <https://doi.org/10.3233/JAE-180021>

5. Boltachev GS, Lukyashin KE, Shitov VA, Volkov NB (2013) Three-dimensional simulations of nanopowder compaction processes by granular dynamics method. *Phys Rev E* 88(1):012209. <https://doi.org/10.1103/PhysRevE.88.012209>
 6. Mamalis AG, Vottea IN, Manolakos DE (2002) Fabrication of metal/sheathed high-Tc superconducting composites by explosive compaction/cladding: numerical simulation. *Mater Sci Eng B* 90(3):254–260. [https://doi.org/10.1016/S0921-5107\(01\)00913-8](https://doi.org/10.1016/S0921-5107(01)00913-8)
 7. Mamalis AG, Vottea IN, Manolakos DE (2006) Development of numerical modelling to simulate the explosive compaction/cladding of YBCO ceramic powders. *Model Simul Mater Sci Eng* 14(2):313–329. <https://doi.org/10.1088/0965-0393/14/2/013>
 8. Han LH, Elliott JA, Bentham AC, Mills A, Amidon GE, Hancock BC (2008) A modified Drucker-Prager Cap model for die compaction simulation of pharmaceutical powders. *Int J Solids Struct* 45(10):3088–3106. <https://doi.org/10.1016/j.ijsolstr.2008.01.024>
 9. Zhou R, L-h Z, He B-y, Y-h L (2013) Numerical simulation of residual stress field in green power metallurgy compacts by modified Drucker-Prager Cap model. *Trans Nonferrous Metals Soc China* 23(8):2374–2382. [https://doi.org/10.1016/S1003-6326\(13\)62744-2](https://doi.org/10.1016/S1003-6326(13)62744-2)
 10. Hu J, Li D, Zhou B, Cui L, Liu Z (2017) Study on numerical simulation of W-Cu20 powder rolling based on Drucker-Prager/Cap model. *Powder Metall Technol* 35(4):249–254
 11. Zhou M, Huang S, Hu J, Lei Y, Xiao Y, Li B, Yan S, Zou F (2017) A density-dependent modified Drucker-Prager Cap model for die compaction of Ag57.6-Cu22.4-Sn10-In10 mixed metal powders. *Powder Technol* 305:183–196. <https://doi.org/10.1016/j.powtec.2016.09.061>
 12. Zhou M, Huang S, Hu J, Lei Y, Zou F, Yan S, Yang M (2017) Experiment and finite element analysis of compaction densification mechanism of Ag-Cu-Sn-In mixed metal powder. *Powder Technol* 313:68–81. <https://doi.org/10.1016/j.powtec.2017.03.015>
 13. Mamalis AG, Manolakos DE, Kladas AG, Koumoutsos AK (2006) Electromagnetic forming tools and processing conditions: numerical simulation. *Mater Manuf Process* 21(4):411–423. <https://doi.org/10.1080/10426910500411785>
 14. Mu L, Hu W, Tao J (2017) Research on compression mechanical properties and constitutive model of nylon. *China Meas Test* 43(11):129–133
 15. Cullen GW (2016) Ductility of 304 stainless steel under pulsed uniaxial loading. University of New Hampshire, Durham
 16. Kabert BA (2011) High strain rate consolidation and forming of Armstrong and HDH titanium powder and sheet material. The Ohio State University
- Publisher's note** Springer Nature remains neutral with regard to jurisdictional claims in published maps and institutional affiliations.